Acta Pharmaceutica Sinica B 2025;15(9):4900−4916

Chinese Pharmaceutical Association
Institute of Materia Medica, Chinese Academy of Medical Sciences

Acta Pharmaceutica Sinica B

www.elsevier.com/locate/apsb
www.sciencedirect.com

ORIGINAL ARTICLE

Intercellular communication interference through energy metabolism-related exosome secretion inhibition for liver fibrosis treatment

Mengyao Zhang[a], Huaqing Jing[a], Xinyi Liu[a], Valentin A. Milichko[c], Yunsheng Dou[a], Yingzi Ren[a], Zitong Qiu[a], Wen Li[a], Weili Liu[b,*], Xinxing Wang[b,*], Nan Li[a,*]

[a]*Tianjin Key Laboratory of Drug Delivery & High-Efficiency, School of Pharmaceutical Science and Technology, Faculty of Medicine, Tianjin University, Tianjin 300072, China*
[b]*Tianjin Institute of Environmental and Operational Medicine, Tianjin 300050, China*
[c]*School of Physics and Engineering, ITMO University, St. Petersburg 197101, Russia*

Received 29 January 2025; received in revised form 6 March 2025; accepted 18 April 2025

KEY WORDS

Liver fibrosis;
Intercellular communication interference;
Energy metabolism;
Exosomes;
Activated hepatic stellate cells;
Quiescent hepatic stellate cells;
Paeoniflorin;
Cu/ZIF-8

Abstract As activated hepatic stellate cells (aHSCs) play a central role in fibrogenesis, they have become key target cells for anti-fibrotic treatment. Nevertheless, the therapeutic efficiency is constrained by the exosomes they secrete, which are linked to energy metabolism and continuously stimulate the activation of neighboring quiescent hepatic stellate cells (qHSCs). Herein, an intercellular communication interference strategy is designed utilizing paeoniflorin (PF) loaded and hyaluronic acid (HA) coated copper-doped ZIF-8 (PF@HA-Cu/ZIF-8, PF@HCZ) to reduce energy-related exosome secretion from aHSCs, thus preserving neighboring qHSCs in a quiescent state. Simultaneously, the released copper and zinc ions disrupt key enzymes involved in glycolysis to reduce bioenergy synthesis in aHSCs, thereby promoting the reversion of aHSCs to a quiescent state and further decreasing exosome secretion. Therefore, PF@HCZ can effectively sustain both aHSCs and qHSCs in a metabolically dormant state to ultimately alleviate liver fibrosis. The study provides an enlightening strategy for interrupting exosome-mediated intercellular communication and remodeling the energy metabolic status of HSCs with boosted antifibrogenic activity.

*Corresponding authors.
E-mail addresses: liuweili-002@163.com (Weili Liu), wxxemail@sina.cn (Xinxing Wang), linan1985@tju.edu.cn (Nan Li).

Peer review under the responsibility of Chinese Pharmaceutical Association and Institute of Materia Medica, Chinese Academy of Medical Sciences.

https://doi.org/10.1016/j.apsb.2025.07.008

1. Introduction

Liver fibrosis arises from a multitude of chronic injuries and often progresses to portal hypertension, cirrhosis, liver failure, and hepatocellular carcinoma[1-4]. To date, no antifibrotic therapy has been approved, while the only available treatment for patients with advanced stages of liver fibrosis is liver transplantation[5]. During the process of fibrogenesis, the transformation of qHSCs to aHSCs is a main driving force of liver fibrosis pathogenesis, which is often accompanied by upregulated energy metabolism and increased extracellular matrix expression[6,7]. As aHSCs play a central role in fibrogenesis, they have become key target cells for anti-fibrotic treatment[6]. Nevertheless, the therapeutic efficiency is constrained by the enhanced intercellular communication between aHSCs and neighboring quiescent qHSCs, which perpetually instigates the rapid activation of the latter. As nanoscale lipid bilayer vesicles secreted by the majority of cells, exosomes play an essential role in intercellular communication and information exchange both basally and under pathological conditions, which have been found to participate in the biological processes of HSC activation[8-13]. Compared with the normal physiological state, the secretion and cargo sorting of exosomes from aHSCs undergo alterations, leading to variations in quantity and quality, while the upregulated secretion of exosomes also reflects the phenotypic transition from qHSCs to aHSCs[10,14-16]. Besides, exosomes derived from aHSCs exhibit elevated concentrations of proteinaceous constituents, which play a pivotal role in the perpetuation of fibrotic cascades[17].

Studies have implicated that exosomal protein molecules from aHSCs encompass glycolytic markers, such as pyruvate kinase M2 (PKM2) and glucose transporter 1 (GLUT1), which are transferred among neighboring qHSC to affect the metabolic switch, continuously inducing the rapid activation of neighboring qHSCs and the significant progression of liver fibrosis[10,18]. What's more, hypoxia-inducible factor (HIF-1) has been linked to the upregulation of energy metabolism-related exosome secretion[18,19]. Thus, inhibiting HIF-1 can be a practical approach to interfere with exosome-mediated intercellular communication, which decreases the secretion of energy metabolism-related exosomes to shield qHSCs from their interference and maintain a metabolically dormant state.

Although preventing the rapid activation of qHSCs could slow down the progression of liver fibrosis, the aHSCs already present in the liver fibrotic matrix persistently secrete extracellular matrix components, thereby exacerbating the deterioration of the disease. Hence, it is imperative to induce aHSCs to return to a metabolically dormant state at the same time. It is reported that activation of HSCs is dependent upon induction of aerobic glycolysis, which provides high bioenergy to meet the elevated biosynthesis and secretion requirements of disease state[20,21]. In addition, the occurrence of glycolysis leads to the accumulation of intracellular lactate, which is associated with the severity of liver fibrosis[4,20]. Current research has yielded several small molecule glycoclastic enzyme inhibitors, such as 3−Bromopyruvate (hexokinase (HK) inhibitor) and Chalcones (phosphofructokinase inhibitor)[22-24]. In addition, some biological metal ions, such as copper ions (Cu^{2+}), exhibit a strong inhibitory effect on HK[25]. Furthermore, zinc ions (Zn^{2+}) are capable of modulating the intracellular lactate dehydrogenase (LDH) activity, potentially through suppression of its enzymatic function or facilitation of its efflux from the cellular compartment[26,27]. Considering the promising hepatoprotective potential of zinc ions and the common zinc deficiency observed in patients with chronic liver diseases [28,29], ion therapy may be a suitable approach.

Herein, we developed an intercellular communication interference strategy to enhance anti-fibrogenic therapy utilizing Paeoniflorin (PF) loaded and hyaluronic acid (HA) modified Cu-doped ZIF-8 (PF@HA-Cu/ZIF-8, PF@HCZ), which could inhibit energy metabolism-related exosomes secretion, thereby maintaining both qHSCs and aHSCs in a low-energy quiescent state (Scheme 1). Firstly, PF@HCZ could selectively target the upregulated CD44 on the surface of aHSCs due to specific interaction, triggering CD44-mediated endocytosis and bioaccumulation in the lesion[30]. Upon taken by lysosomes, the acidic conditions would lead to the degradation of Cu/ZIF-8 and release the encapsulated PF, which could further reduce the secretion of energy-related exosomes by inhibiting HIF-1α, thereby disrupting exosome-mediated intercellular communication and prevent the activation of qHSCs[31]. Simultaneously, the released copper and zinc ions would respectively block HK and LDH in the process of glycolysis, further leading to reduced bioenergetics and prompting aHSCs to revert to the quiescent state. Therefore, PF@HCZ can ultimately maintain both qHSCs and aHSCs in a metabolically dormant state, thereby interrupting the exosome-induced activation cascade of HSCs to halt the progression of liver fibrosis[32]. Overall, we anticipated the exosome-mediated intercellular communication interference strategy, by which remodeling the energy metabolic status at the disease site, will enrich the therapeutic methods available for anti-hepatic fibrosis treatment.

2. Materials and methods

2.1. Materials and reagents

Zinc nitrate hexahydrate ($Zn(NO_3)_2\cdot 6H_2O$) was obtained from Aladdin Chemistry Co., Ltd. (Shanghai, China). Copper (II) nitrate hemipentahydrate ($Cu(NO_3)_2\cdot 2.5H_2O$), olive oil, and carbon tetrachloride (CCl_4) were purchased from Macklin Reagent Co., Ltd. (Shanghai, China). 2-Methylimidazole ($C_4H_6N_2$, 2-MIM), PF, and HA (MW = 5000) were gained from Heowns Science Co., Ltd. (Tianjin, China). Cetyltrimethylamine bromide (CTAB), fluorescein 5−isothiocyanate (FITC), Lyso-tracker red, Hoechst 33342, PKH26, DAPI, FITC-labeled phalloidin peptide, and phosphate-buffered saline (PBS) were bought from Solarbio Science & Technology Co., Ltd. (Beijing, China). The Trypsin−EDTA, Dulbecco's modified Eagle's medium (DMEM), Roswell Park Memorial Institute 1640 (RPMI-1640), Hank's balanced salt solution (HBSS), and penicillin/streptomycin were purchased from Gibco (Waltham, MA, USA). The fetal bovine serum (FBS) was purchased from Pricella Biotechnology Co., Ltd. (Wuhan, China). The lipopolysaccharide (LPS) was bought from

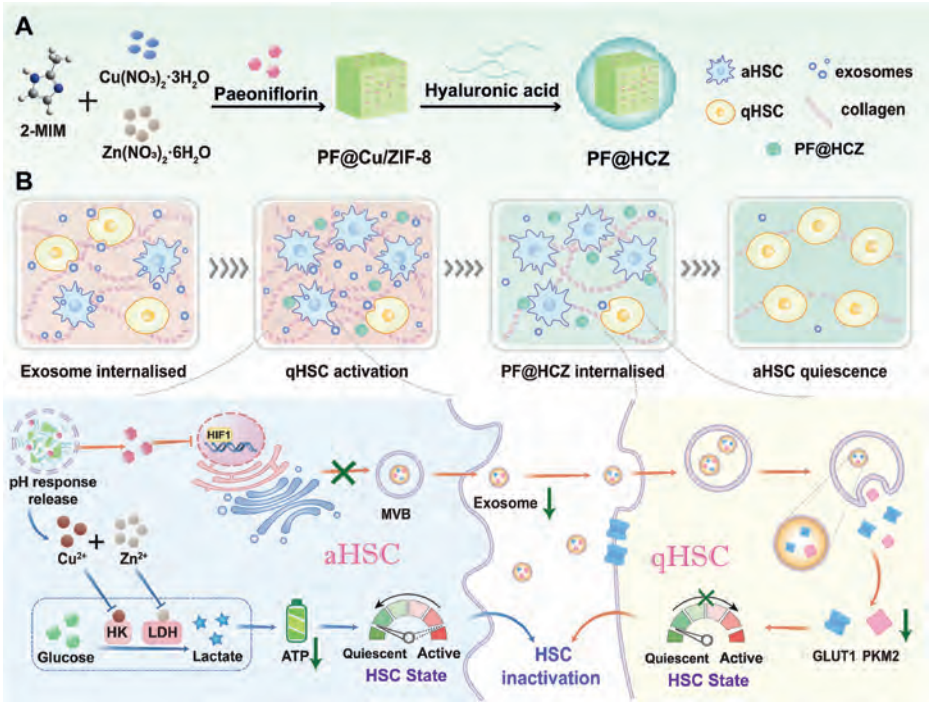

Scheme 1 Preparation and therapeutic mechanism of PF@HCZ for hepatic fibrosis treatment. (A) Synthesis process of PF@HCZ. (B) Mechanism of PF@HCZ treats hepatic fibrosis by regulating metabolism-related exosome secretion and HSCs energy metabolism.

Beyotime Biotechnology (Shanghai, China). Exosome-depleted FBS was obtained from NEWZERUM Ltd. (Christchurch, New Zealand). Rhodamine-labeled wheat germ agglutinin (WGA) and DiR were gained from Maokang Biotechnology Co., Ltd. (Shanghai, China) and Uelandy Biotechnology Co., Ltd. (Suzhou, China), respectively.

2.2. *Preparation of PF@HCZ*

Initially, a classical one-pot solution method was employed to prepare Cu/ZIF-8 loaded with PF (PF@Cu/ZIF-8, PF@CZ), leveraging the porous structure of metal−organic frameworks[33-35]. Specifically, solution A was formulated by dissolving 930 mg of $Cu(NO_3)_2 \cdot 2.5H_2O$, 187.5 mg of $Zn(NO_3)_2 \cdot 6H_2O$, and 10 mg of CTAB in 10 mL of double distilled water (DD H_2O). Then, 4.54 g of 2-MIM and 200 mg PF were thoroughly dissolved in 70 mL of DD H_2O to yield a uniform solution B. Solution A was slowly dripped into Solution B under vigorous stirring and ice-bathing conditions for 50 min. The resulting precipitate was gathered through centrifugation, subsequently washed several times with ethanol, and finally dried overnight in an oven at 50 °C to obtain the brownish PF@CZ.

Subsequently, to modify HA on the surface of PF@CZ, the as-synthesized PF@CZ were dispersed in 75 mL of DD H_2O, followed by the addition of 50 mL of a 5 mg/mL hyaluronic acid solution and subsequent stirring for 2 h. The PF@HCZ was collected by centrifuging (12,000 rpm, 10 min, TG16-WS, Cence, Changsha, China) and washed for three times[36].

2.3. *Characterization of PF@HCZ*

Scanning electron microscope (SEM, Nova Nanosem 430, FEI, Hillsboro, OR, USA) analysis and transmission electron microscopy (TEM, Tecnai G2 F20, Philips, Amsterdam, Netherlands) analysis were carried out to observe the morphology of PF@CZ and PF@HCZ. The elemental composition of PF@HCZ was performed by energy-dispersive X-ray spectroscopy (EDS, EDAX Inc., Mahwah, NJ, USA). The TEM sample was prepared by depositing a small quantity of the sample solution onto 200-mesh molybdenum TEM grids, which were pre-coated with a thin layer of amorphous carbon films. Elemental valence states of Cu/ZIF-8 were determined using X-ray photoelectron spectroscopy (XPS) conducted on the ESCALAB-Xi instrument (Thermo Fisher Scientific, Waltham, MA, USA). X-ray diffraction (XRD) was acquired using a MiniFlex600 General Area Detector (Rigaku Corporation, Tokyo, Japan). Absorption analysis was carried out employing a double-beam UV−Vis spectrophotometer (CARY 60) from Agilent Technologies (Santa Clara, CA, USA). Fourier-transform infrared (FT-IR) spectroscopic analysis was performed utilizing a Tensor 27 infrared spectrophotometer (Bruker Corporation, Billerica, MA, USA), covering the spectral range of 4000−400 cm^{-1}. Measurements of zeta potentials and hydrodynamic diameters were conducted using a dynamic light scattering (DLS) instrument, specifically the Zetasizer Nano ZS (Malvern Panalytical, Malvern, UK). Thermogravimetry analyses (TGA) were performed by Thermogravimetric Analyzer TG 209 F3Tarsus (NETZSCH, Selb, Germany).

2.4. *Measurement of pH-triggered release*

For assessing the pH-responsive release, PF@HCZ (15 mg) was suspended in PBS solutions at pH levels of 5.5, 6.5, and 7.4 and then subjected to dialysis in PBS of the respective pH values. Following the collection of 1 mL of supernatant from the external solution at various time points, the concentration of PF was determined using UV−Vis spectrophotometry, while Zn^{2+} and

Cu^{2+} were analyzed by Zinc Colorimetric Assay Kit and Copper Colorimetric Assay Kit (Elabscience Biotechnology Co., Ltd., Wuhan, China), respectively.

2.5. Cell cultures

The human HSC line LX-2 was purchased from Procell (Wuhan, China), while the human hepatocyte cell line HepaRG was procured from Gibco (Waltham, MA, USA). LX-2 and HepaRG cells were individually cultured in DMEM and RPMI-1640, each enriched with 10% (*v*/*v*) FBS and 1% penicillin−streptomycin, under a humidified atmosphere of 5% CO_2 at a temperature of 37 °C.

2.6. Cytotoxicity examination of PF@HCZ

The assessment of cytotoxicity was conducted on LX-2 and HepaRG cell lines utilizing the CCK-8 Assay Kit (GlpBio Chemicals, Montclair, CA, USA). In brief, the two cell lines were inoculated into 96-well plates with an initial seeding density of 1×10^4 cells per well. Subsequently, the cells were exposed to varying concentrations of PF@HCZ (0, 2.5, 5, 10, and 20 μg/mL). After a 24-h incubation, the cells were exposed to CCK-8 solution (10 μL) diluted in fresh medium (90 μL) and incubated for an additional hour at 37 °C to assess absorbance at 450 nm. Each experimental condition was replicated four times to ensure consistency and reliability.

2.7. Hemolytic activity of PF@HCZ

The study of hemolytic activity was conducted utilizing freshly collected whole-blood samples from mice. Erythrocytes were collected by centrifuging the blood samples at 2000 rpm (Cence) for 10 min, followed by gentle washing three times. Subsequently, a 200 mL erythrocyte suspension was blended with 1 mL PF@HCZ at concentrations of 2.5, 5, 10, 20, and 40 μg/mL. The samples were then incubated at 37 °C for 2 h, centrifuged at 12,000 rpm (Cence) for 15 min, and quantified by assessing the absorbance at 570 nm. PBS was utilized to establish the negative control condition. Conversely, distilled water was employed to define the positive control condition. The hemolysis ratio was determined using the formula provided below, as shown in Eq. (1):

$$\text{Hemolysis}\ (\%) = \frac{A_{\text{Sample}} - A_{(-)}}{A_{(+)} - A_{(-)}} \times 100 \quad (1)$$

2.8. Cellular internalization of PF@HCZ

The intracellular localization of PF@HCZ was examined using a confocal laser scanning microscope (CLSM). To capture CLSM images, LX-2 cells were cultured in confocal dishes at a density of 1×10^5 cells/dish for 24 h. Then, the cells were treated with 10 μg/mL FITC-labeled PF@HCZ. At predetermined time intervals, the cells were stained with Hoechst 33342 and Lyso-tracker red to visualize by CLSM Leica SP 8 (Leica, Wetzlar, Germany).

2.9. Metabolite activity and ATP level measurement

In the therapeutic study, LX-2 cells were incubated with DMEM (Control) (G1), LPS (G2), LPS + 1.5 μg/mL PF (G3), LPS + 8.5 μg/mL HZ (G4), LPS + 8.5 μg/mL HCZ (G5), and LPS + 10 μg/mL PF@HCZ (G6). The concentrations of HK and lactate were determined by the Micro Hexokinase Activity Assay Kit or Micro Lactate Assay Kit, which was provided by Abbkine Biotechnology Co., Ltd. (Wuhan, China). Lactate Dehydrogenase Activity Assay Kit (Solarbio Science & Technology Co., Ltd., Beijing, China) was employed to measure the level of LDH, while adenosine 5′-triphosphate (ATP) was quantified by ATP Assay Kit from Beyotime Biotechnology (Shanghai, China). All the measurements were executed in strict adherence to the protocols specified by the manufacturers. The content of alpha-smooth muscle actin (α-SMA) was determined using an α-SMA enzyme-linked immunosorbent assay (ELISA) kit (Jonln Biotechnology, Shanghai, China). The levels of HK, LDH, lactate, ATP, and α-SMA were normalized to protein concentrations in each sample. Fluorescence data were acquired with a multifunctional plate reader (FlexStation 3, Molecular Devices, San Jose, CA, USA).

2.10. Exosome extraction from LX-2 cells

Exosomes were isolated from the culture supernatant of LX-2 cells. In brief, LX-2 cells were propagated in a medium supplemented with exosome-depleted FBS over an extended period, followed by LPS induction and administration of different treatments (PF 1.5 μg/mL, HZ 8.5 μg/mL, HCZ 8.5 μg/mL, and PF@HCZ 10 μg/mL). The supernatants from the cell cultures were harvested and subjected to centrifugation at 2000×*g* for 30 min at 4 °C (Heraeus Multifuge X1R, Thermo Fisher Scientific, Waltham, MA, USA) to pellet cells, followed by further centrifugation at 10,000×*g* (Thermo Fisher Scientific) for an additional 30 min to remove residual cellular debris. The supernatant was subjected to filtration using a 2 μm filter, and then exosomes were extracted using the exosomes/EVs isolation system (EXODUS H1+AS, Huixin Biotechnology, Shenzhen, China). The pelleted exosomes were resuspended with 400 μL PBS.

2.11. Characterization of exosomes

The characterization of exosomes was conducted in accordance with the Minimal Information for Studies of Extracellular Vesicles 2018 (MISEV 2018) guidelines proposed by the International Society for Extracellular Vesicles (ISEV)[37]. The concentration of protein within the exosome was determined by employing a BCA Protein Assay Kit (GlpBio Chemicals, Montclair, CA, USA) in strict accordance with the procedural directives furnished by the manufacturer. Exosomes were visualized using TEM (Philips). In a concise procedure, exosomes (10 μL) were spread onto a 200-mesh copper grid for a duration of 50 min. Then, negative staining was carried out using ammonium molybdate. In addition, nanoparticle tracking analysis (NTA) was conducted using NanoSight Pro (Malvern Panalytical, Malvern, UK).

2.12. Western blot analysis of cell and exosomes

The Western blot technique was employed to assess the expression levels of Collagen-I, α-SMA, and HIF-1α in LX-2 cells post-treatment, as well as PKM2 and GLUT1 in exosomes. For the cell Western blot experiments, 1×10^6 LX-2 cells per dish were initially seeded and cultured with different treatments for 24 h. Subsequently, the cells were lysed using RIPA lysis buffer supplemented with PMSF (Solarbio Science & Technology Co., Ltd., Beijing, China), while the quantification of the total protein content within cellular lysates was ascertained employing a BCA

Protein Assay Kit (GlpBio Chemicals) following harvesting. The samples were diluted in protein loading buffer and boiled for 5 min before loading onto the sodium dodecyl sulfate-polyacrylamide gel electrophoresis (SDS-PAGE) and subsequently blotted onto polyvinylidene fluoride (PVDF) membranes. The PVDF membranes were blocked with 5% dry milk in TBST for 1.5 h, followed by incubation with anti-β-actin antibody (1:1500, Signalway Antibody, Rockville, MD, USA), anti-−HIF−1α antibody (1:800), anti-α-SMA antibody (1:1500), and anti-collagen-I antibody (1:1500) from Beyotime Biotechnology (Shanghai, China). Next, the membrane was thoroughly washed with TBST and incubated with Goat Anti-Rabbit IgG secondary antibody horse radish peroxidase (HRP) conjugated (1:10,000, Signalway Antibody, Rockville, MD, USA) or Goat Anti-Mouse IgG secondary antibody HRP conjugated (1:8000, GenScript Biotech Corporation, Piscataway, NJ, USA) at room temperature for 1 h. Finally, the proteins were visualized using a Chemiluminescent Western Blot Imaging System (Azure 300, Azure Biosystems, Pleasanton, CA, USA).

In accordance with the exosome Western blot experimental procedure, the isolated exosomes were combined with a loading buffer and subjected to a 40-min incubation at 37 °C in a water bath. Subsequently, the samples were resolved through SDS-PAGE and transferred onto a PVDF membrane. To prevent non-specific binding, the membrane was then blocked with a 5% milk solution for 1.5 h. The antibodies employed include the anti-CD9 antibody (1:1500, Affinity Bioscience, Changzhou, China), anti-TSG101 antibody (1:2000, Affinity Bioscience, Changzhou, China), anti-Calnexin antibody (1:5000, Beyotime Biotechnology, Shanghai, China), anti-PKM antibody (1:1500, Beyotime Biotechnology, Shanghai, China), anti-GLUT1 antibody (1:2000, Proteintech, Wuhan, China), as well as the HRP-conjugated secondary antibody mentioned above.

2.13. PKH26-labeled exosome internalization

PKH26 was utilized for exosome labeling under the manufacturer's instruction. After co-incubating 200 μL exosomes with 2 μL PKH26 dye for 3 min, the exosomes/EVs isolation system was used to remove unbound dye. Subsequently, PKH26-labeled exosomes were co-cultured with LX-2 cells for 2−24 h, followed by labeling the cytoskeleton and cell nucleus with FITC-labeled phalloidin peptide and Hoechst 23342, respectively. Finally, we observed the red signals of PKH26-labeled exosome *via* CLSM (Leica).

2.14. Cellular immunofluorescence

When co-culturing exosomes with cells, a total of 20 mg of exosomes from LX-2 cells pre-treated with different treatments were added to the culture medium of the receptor cells seeded in a confocal dish. The cells were rinsed with PBS three times, treated with 4% paraformaldehyde for fixation, and blocked using an immunostaining blocking solution. Rhodamine-WGA at a concentration of 5 μg/mL in HBSS was utilized to label the cell membrane for 15 min, followed by another round of PBS washing. Subsequent permeabilization with Triton X-100 (0.2%) for 15 min facilitated antibody penetration. The cells were subjected to overnight incubation at 4 °C with a primary antibody specific for PKM2 or GLUT1 at a dilution of 1:200. After PBS rinsing, they were subsequently incubated with a FITC-labeled secondary antibody for 1 h at ambient temperature. Hoechst 23342 staining for 15 min was performed to visualize the nuclei, which offered a comprehensive understanding of cellular morphology and the distribution of specific markers.

2.15. Induction of liver fibrosis in mice

Female BALB/c mice were purchased from Huafukang Biological Technology Co., Ltd. (Beijing, China) and housed in a controlled environment with monitored temperature and humidity levels with the institutional guidelines for Care and Use of Laboratory Animal Experience of Tianjin University. All animal experiments were approved by the Medical Ethics Committee of Peking Union Medical College. Hepatic fibrosis in mice was induced by administering intraperitoneal injections of a CCl_4 solution (2 mL/kg, mixed with olive oil at a 1:9 ratio) twice weekly over 8 weeks. The healthy mice received an equivalent volume of olive oil as the control group.

2.16. Treatment strategy of liver fibrosis in mice

In the therapeutic study, mice with induced hepatic fibrosis received biweekly treatments for 4 weeks with the subsequent samples: PF (2 mg/kg), HA-ZIF-8 (HZ) (10 mg/kg), HA-Cu/ZIF-8 (HCZ) (10 mg/kg), and PF@HCZ (12 mg/kg). Each sample was separately dissolved in physiological saline and then injected intravenously into the mice. Both the control and fibrotic groups were administered an equal volume of saline *via* intravenous injection.

2.17. In vivo and ex vivo biodistribution

In the tissue biodistribution research, DiR-loaded PF@HCZ nanocarriers were intravenously injected into both fibrotic and healthy mice. The PF@CZ solution was stirred with DiR for 24 h and collected by centrifugation (12,000 rpm, 10 min, Cence). Subsequently, the DiR-loaded PF@HCZ nanocarriers were coated with HA following a previously established protocol. Finally, the DiR-loaded PF@HCZ nanocarriers were administered 10 mg/kg to healthy and fibrotic mice, respectively. At 4, 8, and 12 h, as well as on Days 1, 2, 4, 6, and 8 post-injections, the mice were anesthetized through intraperitoneal injection of tribromoethanol and then were subjected to *in vivo* fluorescence imaging using the IVIS Spectrum system (PerkinElmer, Waltham, MA, USA). Additionally, on 12 h, Days 1, 3, 6, and 8 post-injections, the mice were subjected to euthanasia for the procurement of major organs to conduct *ex vivo* imaging analyses.

2.18. Intrahepatic cell-type-specific distribution and targeting ability evaluation

The intracellular localization within the liver of mice was further explored using DiR-loaded PF@HCZ nanocarriers. These nanocarriers were administered to mice with both normal and fibrotic conditions. After the last dose, the animals were sacrificed 24 h post-injection to obtain liver tissues for paraffin embedding. The liver tissues were stained with albumin from Biogot Technology, Co., Ltd. (Nanjing, China) or α-SMA antibody from Bioss (Beijing, China), followed by overnight incubation at 4 °C. Following rinsing, the tissues were incubated with a FITC-conjugated secondary antibody (ZSGB-Bio Co., Ltd., Beijing, China), then counterstained with DAPI, visualized under fluorescence microscopy.

2.19. Anti-fibrosis efficiency in vivo

In the efficacy assessment of the treatment, mice were categorized into six groups as follows: G1: Healthy, G2: CCl_4, G3: CCl_4 + PF, G4: CCl_4 + HZ, G5: CCl_4 + HCZ, G6: CCl_4 + PF@HCZ. Following the final treatment, all mice were subjected to euthanasia at 48 h post-intervention, after which a comprehensive necropsy was performed to harvest major organs and collect blood samples for subsequent *ex vivo* analyses. The harvested organs were then rinsed with 3 mL of paraformaldehyde solution, a standard fixative employed in histological studies. In addition to histological analysis, a variety of biomedical analyses and measurements, including biochemical analysis and relevant biomedical evaluations, were conducted on the procured organs and blood samples.

2.20. Immunofluorescence and histological staining

The liver tissues preserved in paraformaldehyde were utilized for immunofluorescence staining. Liver tissues from various treatment groups were subjected to a careful processing protocol. First, dehydrate the tissues with ethanol before embedding them in paraffin to ensure ideal conditions for subsequent analyses. Subsequently, the liver tissues were subjected to staining with Hematoxylin and Eosin (H&E), Masson's trichrome, Sirius Red, immunohistochemical (IHC) staining for α-SMA and collagen-1 antibodies, as well as immunofluorescence staining for HIF-1α and double staining of GFAP with GLUT1 or PKM2. To ascertain the quantification of immunostaining data, the intensity of positive signals was analyzed employing ImageJ (National Institutes of Health, Bethesda, MD, USA), a standard software tool utilized for quantitative image analysis in biomedical research.

2.21. Exosome extraction from mice liver tissue

The tissues were placed on ice and cut into 1 mm^3 pieces. Next, the tissue samples were treated with 1 mL of Collagenase IV and 5 μL of 200 × DNase I, while the mixture was gently agitated and incubated on a temperature-controlled shaker at 37 °C with a speed of 100 rpm for a duration of 60−90 min. The resulting tissue homogenate was subjected to centrifugation at 3000×*g* (Thermo Fisher Scientific)for 10 min at a temperature of 4 °C, followed by subsequent centrifugation of the supernatant at 12,000×*g* (Thermo Fisher Scientific) for 30 min under the same temperature conditions[38]. After diluting the supernatant with PBS, it was filtered through a 0.22 μm membrane and then collected for exosome extraction with the exosomes/EVs isolation system (Huixin Biotechnology). The collected exosomes were further characterized using techniques such as TEM, NTA, BCA, and Western blot.

2.22. Pharmacokinetics and biosafety study of PF@HCZ

The metabolism and excretion studies of PF@HCZ were conducted using an inductively coupled plasma mass spectrometer (ICP-MS) Agilent 7900 (Agilent Technologies, Inc., Santa Clara, CA, USA). Mice (n = 3) were administered PF@HCZ *via* intravenous injection at a dosage of 12 mg/kg. Blood samples from the ocular globe of the mice were collected at various time points: 0, 2, 4, 6, 8, 12, 24, and 48 h post-injection. The samples were dissolved in nitric acid heated to 100 °C, and the concentrations of Cu and Zn were measured using ICP-MS (Agilent Technologies, Inc.). Additionally, urine and feces were collected at different time points for pharmacokinetic analysis.

To conduct the biosafety study, BALB/c mice (n = 3) were treated biweekly for 8 weeks with the following samples: 1) healthy control, 2) CCl_4 + PF (2 mg/kg), CCl_4 + HZ (10 mg/kg), CCl_4 +HCZ (10 mg/kg), and CCl_4 + PF@HCZ (12 mg/kg). After the treatment period, the mice were euthanized, and blood samples along with major organs (liver, heart, spleen, lungs, and kidneys) were collected for long-term biosafety analysis. Serum alanine aminotransferase (ALT), aspartate aminotransferase (AST), alkaline phosphatase (ALP), total cholesterol (TC), albumin (ALB), creatinine (CREA), uric acid (UA), and urea levels were quantitatively measured using an automated biochemical analyzer.

2.23. Statistical analysis

All data in this study were expressed as mean ± standard deviation (SD). The Student's *t*-test (two-tailed) was employed to analyze the differences, with statistical significance denoted as NS (no significance), $^*P < 0.05$, $^{**}P < 0.01$, $^{***}P < 0.001$, $^{****}P < 0.0001$.

3. Results and discussion

3.1. Synthesis and characterization of PF@HCZ

In this study, the designed bimetallic polymerization network was synthesized *via* a two-step method. First, the synthesis of PF@CZ was accomplished *via* a traditional one-pot methodology, leveraging the porous structure of metal−organic frameworks. This method enclosed Paeoniflorin within the framework to mitigate the risk of drug leakage and simultaneously enhance drug-loading efficiency. As illustrated in the TEM and SEM micrograph (Fig. 1A and Supporting Information Fig. S1), the PF@CZ exhibited cube-like morphology with uniform sizes and homogeneous dispersion. HA is modified onto the surface of PF@CZ by electrostatic interaction, which is attributed to the positively charged surface of Cu/ZIF-8 and the negative charge conferred by the carboxyl groups in HA[39,40]. Following HA modification, the TEM images (Fig. 1B) revealed that the nanocubes were enveloped by a thin layer of HA, while the SEM (Fig. 1C) images also showed a slightly rougher surface of the particles. The average hydrodynamic diameters of PF@CZ and PF@HCZ were approximately 137 and 190 nm, respectively, with the average zeta potential changed from 30.1 to −12.5 mV after modifying (Fig. 1L and Supporting Information Fig. S2), which confirmed the successful enveloping as well as adequate dispersion and uniformity of the nanoplatforms in aqueous solution.

The EDS was carried out (Fig. 1D and Supporting Information Fig. S3) to further investigate the composition of the nanoplatforms, which showed that copper and zinc ions distributed homogeneously with a ratio of ∼1:5. XPS analysis was employed to determine the elemental compositions and valence states of Cu-ZIF-8 (Fig. 1E), which confirmed the dimethylimidazole structure and robust bonding of Cu and Zn elements (Fig. 1I)[41]. The characteristic peaks corresponding to Zn 2p1/2 and Zn 2p3/2 were identified at 1044.75 and 1021.81 eV, respectively (Fig. 1F), indicating that the Zn element was predominantly in ionic (Zn^{2+}) form. Furthermore, the Cu 2p spectrum of Cu/ZIF-8 was displayed in Fig. 1G, in which two peaks of Cu 2p1/2 and Cu 2p3/2 were observed around 953.73 and 933.98 eV with two satellite peaks at

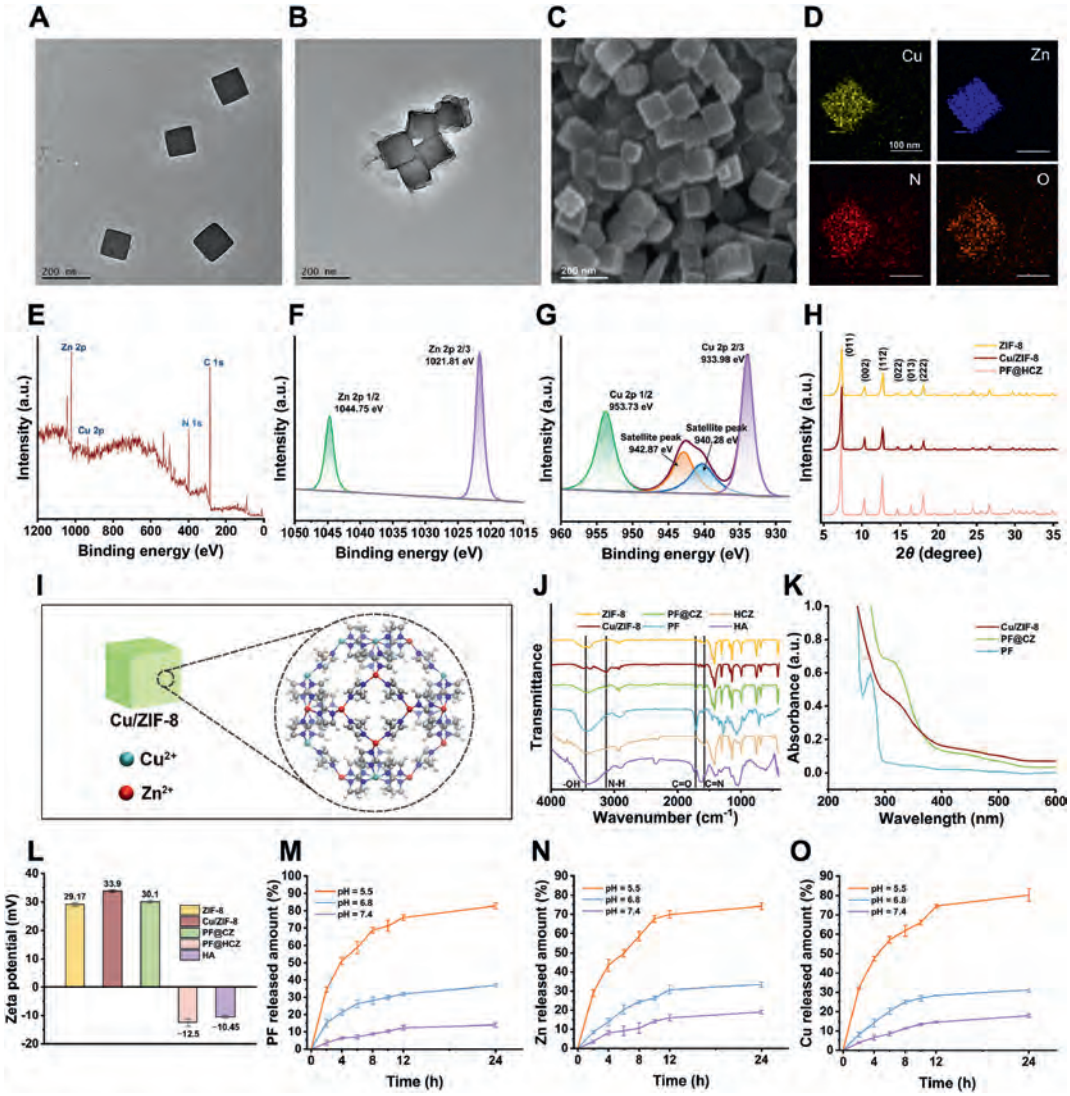

Figure 1 Characterization of PF@HCZ. (A) TEM image of PF@CZ. (B) TEM image of PF@HCZ. (C) SEM image of PF@HCZ. Scale bar = 200 nm (Fig. 1A−C). (D) The corresponding element mapping of PF@HCZ: Cu, Zn, N, and O (scale bar = 100 nm). XPS spectra of Cu/ZIF-8: (E) survey scan; (F) Zn 2p; (G) Cu 2p. (H) X-ray diffraction analysis of ZIF-8, Cu/ZIF-8, and PF@HCZ. (I) Schematic representation of Cu/ZIF-8 crystals. (J) IR-spectra of ZIF-8, Cu/ZIF-8, PF@CZ, PF, HCZ, and HA. (K) UV−Vis spectrums of Cu/ZIF-8, PF@CZ, and PF. (L) Zeta potential of ZIF-8, Cu/ZIF-8, PF@CZ, HA, and PF@HCZ. (M) PF, (N) Zn^{2+}, and (O) Cu^{2+} release curves of PF@HCZ at pH 7.4/6.8/5.5. Data are shown as the mean ± SD (n = 3).

942.87 and 940.28 eV, assigning that Cu was in the +2-valence state[41]. The XRD patterns revealed that the diffraction peaks of the Cu/ZIF-8 sample closely matched the characteristic peak positions of the simulated ZIF-8, indicating that the crystal structure remained unaltered with the presence of Cu^{2+} (Fig. 1H). Due to the minimal difference in ionic sizes between Cu^{2+} (0.72 Å) and Zn^{2+} (0.74 Å) in tetrahedral coordination, the incorporation of Cu^{2+} may not significantly disturb the crystal structure of ZIF-8.

PF, a monoterpene glycoside with the function of inhibiting HIF-1α, was effectively encapsulated into the porous framework of Cu/ZIF-8[42,43]. In the FT-IR spectrum (Fig. 1J), the distinctive hydroxy group of PF and HA at 3417 cm^{-1} was clearly discernible both in the PF@CZ and HCZ samples, indicating the successful load. Subsequently, the characteristic peak in the UV−Vis spectroscopy provided evidence of PF encapsulation, while the observed redshift may be attributed to hydrogen bonding occurring during the encapsulation (Fig. 1K). After the complete degradation of the nanoparticles, the drug loading percentage was estimated to be ~16.5% based on the standard curve (Supporting Information Fig. S4). Furthermore, the modification level of HA was evaluated using TGA (Supporting Information Fig. S5).

In addition, PF@HCZ nanoparticles exhibit the ability to undergo degradation in acidic conditions, leading to the release of Cu^{2+}, Zn^{2+}, and PF. PBS solutions in various pH levels were employed to replicate complex physiological scenarios and validate the pH-responsive degradation of PF@HCZ. After incubation in pH 7.4 buffer for 24 h, the release of PF, Zn^{2+}, and Cu^{2+} was observed to be below 13.90 ± 1.24%, 19.00 ± 1.02%, and 17.86 ± 0.96%, respectively (Fig. 1M−O). In this study, pH 6.8 was utilized to simulate the liver environment under fibrotic conditions, wherein it was observed that PF, Zn^{2+}, and Cu^{2+} were gradually released at this weakly acidic pH, reaching

36.75% ± 0.93%, 33.32% ± 1.42%, 31.30% ± 1.37% release after 24 h, respectively. Conversely, in a pH 5.5 solution, they reached the peaks at 82.83 ± 1.56%, 74.25 ± 1.67%, and 80.24 ± 3.27%, respectively, underscoring the direct relationship between the amount of released PF, reaction duration, and buffer acidity. In this system, copper and zinc ions show comparable release patterns, as they were doped in a similar manner. Notably, PF@HCZ nanoparticles demonstrated a specific and continual degradation in an acidic lysosome environment after cellular internalization, while maintaining relative stability in a physiological environment with a pH of 7.4, which served against premature drug release and reduced adverse effects. Furthermore, the stability of nanoparticles is a focal point that requires attention. PF@HCZ demonstrated good stability, as evidenced by a consistent hydrodynamic diameter over a 7-day incubation period in water and various physiologically relevant fluids such as PBS, culture medium (DMEM), and serum (Supporting Information Fig. S6).

3.2. *Cellular uptake and toxicity of PF@HCZ in vitro*

Encouraged by the above physicochemical properties, we further investigated the biological properties *in vitro*. First, we detected the potential cytotoxicity of PF@HCZ by co-incubating LX-2 or HepaRG cells under different concentrations (0, 2.5, 5, 10, and 20 μg/mL) for 24 h to carry out CCK-8 assay. We found that 20 μg/mL PF@HCZ caused approximately 20% viability decline in LX-2, while it remained over 86 ± 2.75% in HepaRG (Fig. 2B). Moreover, the hemolytic effect on murine erythrocytes at 40 μg/mL was negligible (less than 2.61 ± 0.12%) (Fig. 2C), demonstrating the excellent blood compatibility.

CD44 serves as one of the principal receptors for HA[44]. In healthy liver tissue, the expression of CD44 is minimal, while the expression is significantly upregulated during the progression of liver fibrosis, especially in HSCs[45,46]. As illustrated in Supporting Information Fig. S7, the expression levels of CD44 in LX-2 cells were upregulated following LPS induction. Furthermore, CLSM images demonstrated that the induced LX-2 cells exhibited an enhanced uptake of FITC-labeled PF@HCZ, which is associated with elevated expression levels of CD44 (Supporting Information Fig. S8).

Meanwhile, a time-dependent experiment was conducted employing CLSM (Leica) to examine the cellular uptake process. LPS-pretreated LX-2 cells were exposed to FITC-labeled PF@HCZ for 0, 2, 4, and 8 h. Lyso-tracker red and Hoechst 33342 were utilized to stain the lysosomes and nuclei of LX-2 cells, respectively. At 2 h, a green fluorescent signal was detected, co-localizing with the red signal from the lysosomes within the cells. After 4 h, an increase in the green fluorescence area within the cells was observed, which extensively overlapped with the red lysosomes, confirming the uptake of PF@HCZ through the lysosomes of LX-2 cells. The green signal persisted and escaped from the lysosomes after 8 h, indicating the successful release of PF@HCZ components into the cytoplasm to exert their functions (Fig. 2D).

3.3. *Glycolysis inhibition in aHSCs*

It is reported that the activation of hepatic stellate cells is accompanied by aerobic glycolysis, which induces the production of high levels of bioenergy to meet the high biosynthesis and secretion demands of aHSCs in the disease state[20,21]. In this section, our focus was on elucidating the inhibitory mechanism of PF@HCZ on aHSCs glycolysis (Fig. 2A). In this strategy, the copper and zinc ions released from Cu/ZIF-8 could respectively inhibit the key enzymes HK and LDH involved in the glycolysis process. From the results, the HK level of LPS-pretreated aHSCs decreased by 19.32% and 27.53% following the administration of HCZ and PF@HCZ, respectively, in comparison to the group without treatment (Fig. 2E). Similarly, intracellular LDH levels exhibited a significant increase following LPS induction, whereas the levels in the HZ and PF@HCZ group were only 87.18% and 84.70% of it, respectively (Fig. 2F). In addition, the activation of glycolysis contributes to the intracellular accumulation of lactate, which correlates with the advancement of liver fibrosis. As expected, a gradual reduction of intracellular lactate levels from G2 to G6 was observed (Fig. 2G), which was in accordance with the trend in the ATP level detection experiments (Fig. 2H), further demonstrating the inhibitory effect on bioenergy of PF@HCZ.

Considering the enhanced efficacy in bioenergy suppression, it is imperative to conduct further research on the activities of HSCs, encompassing the processes of HSC activation and collagen synthesis. Here, α-SMA was regarded as a hallmark indicative of HSCs activation for detection. From the results, the expression level of α-SMA and collagen production was significantly reduced in the treated groups, indicating that PF@HCZ induced aHSCs to revert to a relatively quiescent state (Fig. 2I−K). Moreover, the PF@HCZ groups reduced collagen-I production by 77.8% in comparison to the LPS group (G2) (Fig. 2K). Moreover, dose-dependent experiments indicated that the inhibitory effect on α-SMA progressively intensified with increasing dosages. It was observed that the enhancement of the high dose (20 μg/mL) compared to the low dose (5 μg/mL) was ∼24.3%, while the variation between the moderate and high doses was not significant (Supporting Information Fig. S9A). Taken together, the obtained data confirmed that PF@HCZ can inhibit the glycolysis of aHSCs to decrease cellular energy, thereby inducing the transformation of aHSCs into a relatively quiescent state.

3.4. *Inhibitory effect on energy metabolism-related exosomes in vitro*

Further validation is required to confirm the inhibitory effect of PF@HCZ on energy metabolism-related exosomes, which was investigated *in vitro*. This study investigated the levels of HIF-1α in aHSCs after receiving different treatments and extracted extracellular vesicles from their culture medium for subsequent analyses (Fig. 3A and B). It can be observed that, compared to the LPS group (G2), the expression levels of HIF-1α in the PF@HCZ treatment group (G6) decreased by approximately two-thirds, whereas the PF group (G3) exhibited a reduction of about 40% (Fig. 3C and E), which indicated the excellent targeting capability and therapeutic efficacy of the delivery system.

Besides, we extracted extracellular vesicles secreted by LPS-pretreated LX-2 cells from the culture medium after receiving different treatments for further investigation (Fig. 3B). Typical cup-shaped structure vesicles can be clearly observed (Fig. 3F), indicating the successful extraction of extracellular vesicles. Moreover, under the same dilution conditions for sample preparation, a greater number of vesicles were found in the field of view for the LPS group. Compared to the cells, the exosomal markers of TSG101 and CD9 were detected in all exosome groups, while the cell-specific marker of Calnexin (negative control) was only present in the cell group, further confirming the successful extraction

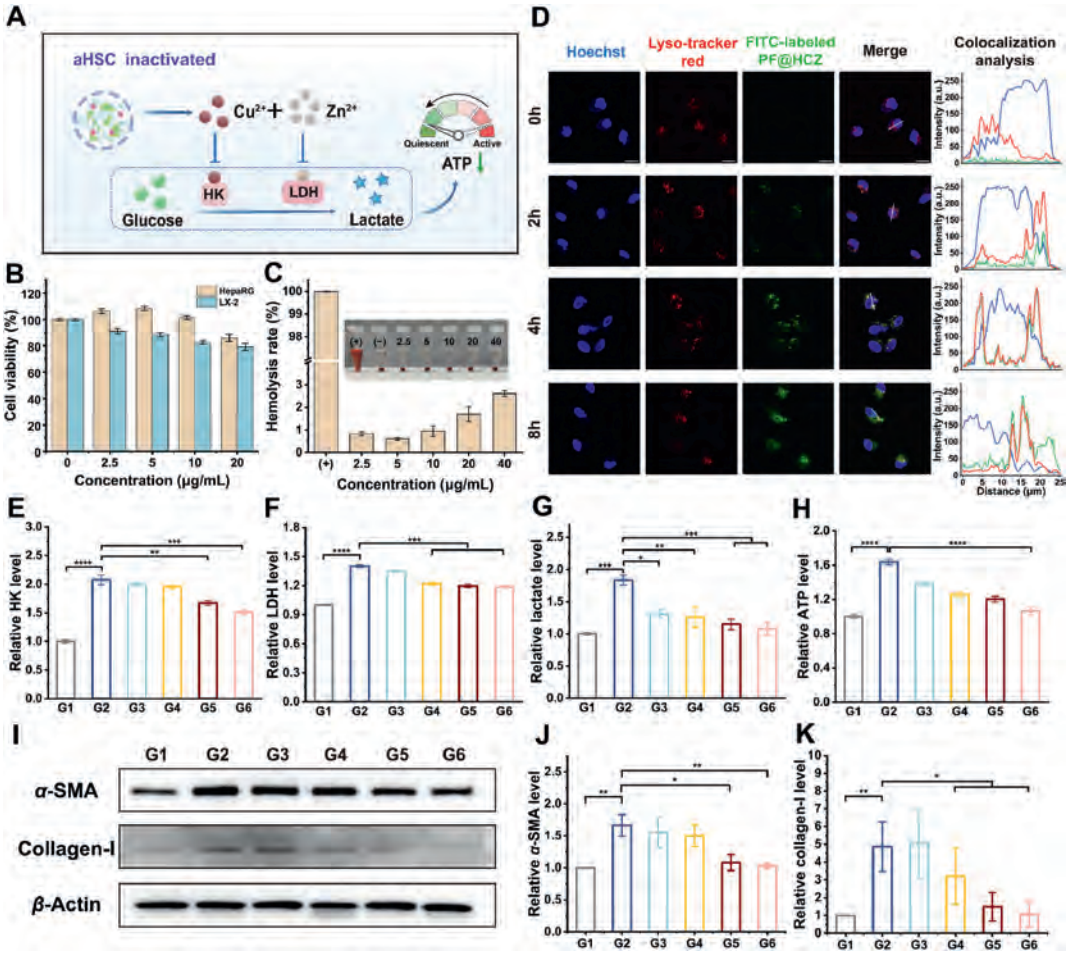

Figure 2 Inhibitory effect on glycolysis *in vitro*. (A) Schematic illustration of the anti-fibrogenic mechanism of PF@HCZ in activated LX-2 cells by inhibiting glycolysis. (B) Viability of LX-2 cells and HepaRG cells treated with different concentrations of PF@HCZ for 24 h ($n = 4$). (C) Hemolytic activity of PF@HCZ in murine erythrocytes. (D) CLSM micrographs showing the kinetics of the cellular uptake of FITC-labeled PF@HCZ by LX-2 cells and their intracellular fate in different time intervals (0, 4, 8, and 12 h). Scale bar = 30 μm. (E) Relative HK level, (F) Relative LDH level, (G) Relative lactate level, and (H) Relative ATP level in LX-2 cells. (I) The expression of α-SMA and collagen-I in LX-2 cells. Quantitative analysis of (J) α-SMA and (K) collagen-I content in Fig. 2I. LX-2 cells were incubated with DMEM (Control) (G1), LPS (G2), LPS + PF (G3), LPS + HZ (G4), LPS + HCZ (G5), and LPS + PF@HCZ (G6). Data are shown as the mean ± SD ($n = 3$). NS (no significance), $^{*}P < 0.05$, $^{**}P < 0.01$, $^{***}P < 0.001$, $^{****}P < 0.0001$.

of extracellular vesicles (Supporting Information Fig. S10). The protein content of the extracted extracellular vesicles was determined using the BCA assay, which revealed a 17.61% and 32.93% reduction in protein content in the PF and PF@HCZ groups, respectively, compared to the model group (Fig. 3D). Moreover, NTA showed a similar trend in particle concentration in the extracellular vesicle suspensions (Fig. 3G).

In Western blot experiments, by using the exosomal marker protein CD9 as a loading control, the levels of GLUT1 and PKM2 in extracellular vesicles from the PF@HCZ group were found to decrease by approximately 41.76% and 53.81%, respectively (Fig. 3H–J). The HZ (G4) and HCZ (G5) groups also exhibited a slight decreasing trend, which is associated with the reduction in energy metabolism of aHSCs, resulting in a certain degree of inhibition of secretion. Therefore, the above experiments confirmed the successful extraction and validated the significant inhibitory effect of PF@HCZ on energy-related extracellular vesicles.

3.5. *Inhibition of qHSCs activation by PF@HCZ in vitro*

Energy metabolism-related extracellular vesicles secreted by aHSCs can be engulfed by qHSCs to release glycolysis-related proteins such as GLUT1 and PKM2, thus leading to enhancement of energy metabolism, subsequently promoting rapid activation of qHSCs (Fig. 4A). Building upon the internal GLUT1 and PKM2 content, this study further investigated the impact of the exosomes on qHSCs by co-incubating the extracted extracellular vesicle from different groups with quiescent LX-2 cells (Fig. 4B). From Fig. 4C, the red signals (PKH26-labeled exosomes) within the cells gradually intensified over time, indicating the excellent engulfment capability of quiescent LX-2 cells.

Subsequently, the impact of extracellular vesicles secreted by activated LX-2 cells was examined. Based on Fig. 4E and F, it can be observed that there was a 2.28 ± 0.36-fold increase in PKM2 levels in LPS-treated cells compared to the control group following co-culture with extracellular vesicles. In the PF group,

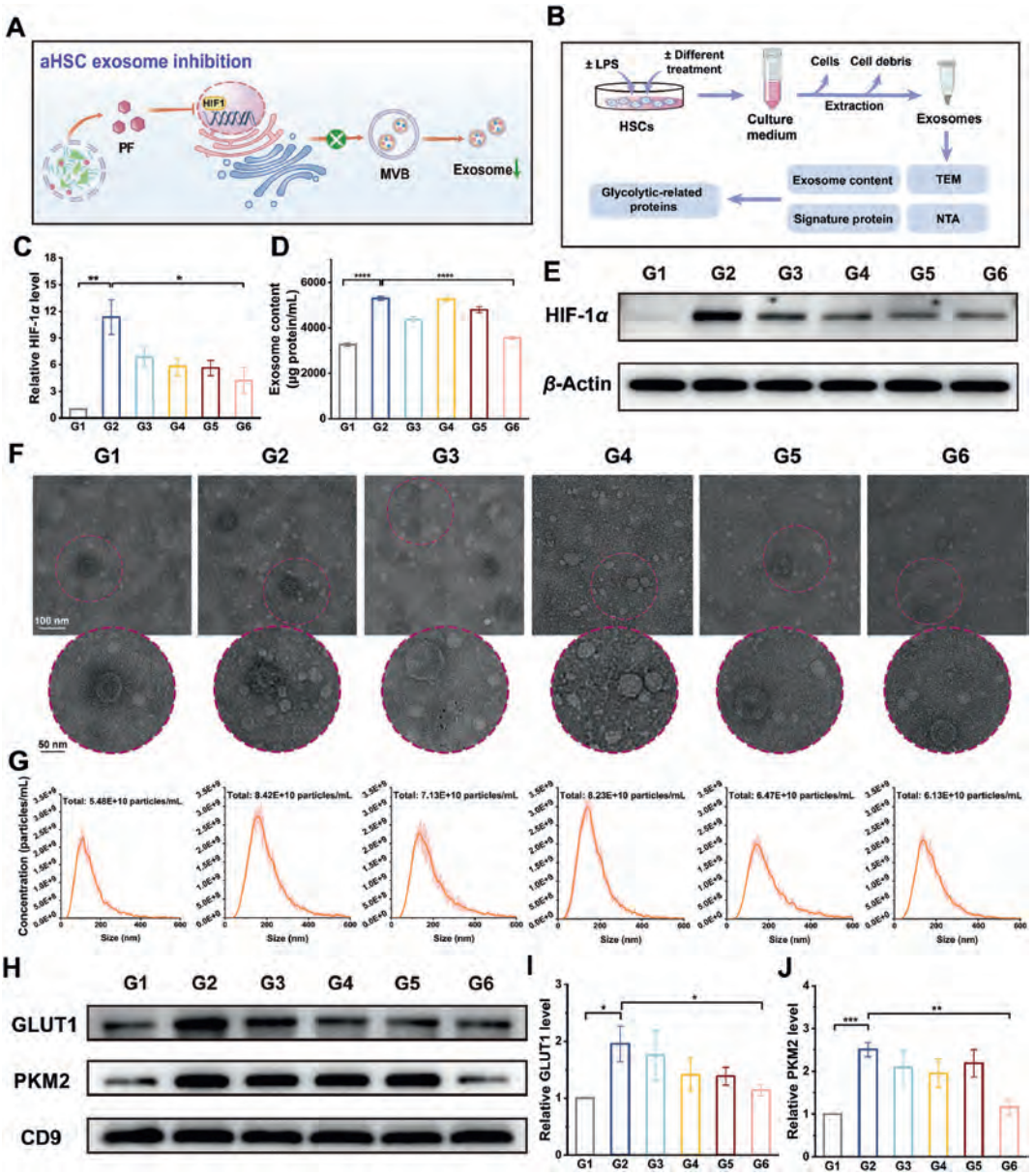

Figure 3 Inhibitory effect on energy metabolism-related exosomes *in vitro*. (A) Schematic illustration of the anti-fibrogenic mechanism of PF@HCZ in LX-2 cells by inhibiting exosome secretion. (B) Illustration of the method for extracting exosomes from LX-2 cells and verifying methods. (C, E) The expression of HIF-1α in LX-2 cells incubated with different treatments. (D) The protein content of the extracted exosomes. (F) TEM image of the extracted exosomes (scale bar = 100 & 50 nm). (G) NTA of exosomes from LX-2 cells. (H) The expression of GLUT1 and PKM2 in the exosomes. Quantitative analysis of (I) GLUT1 and (J) PKM2 content in Fig. 3H. LX-2 cells were incubated with DMEM (Control) (G1), LPS (G2), LPS + PF (G3), LPS + HZ (G4), LPS + HCZ (G5), and LPS + PF@HCZ (G6). Data are shown as the mean ± SD (n = 3). NS (no significance), *P < 0.05, **P < 0.01, ***P < 0.001, ****P < 0.0001.

there was a 1.56 ± 0.04-fold increase, while the PF@HCZ group showed a negligible change. The levels of GLUT1 in the cells exhibited a similar trend, increasing by 1.50 ± 0.07-fold in the LPS group and only 1.06 ± 0.03-fold in the PF@HCZ group as opposed to the control group (Fig. 4G and H). However, the contents of exosomes are highly complex. To investigate whether PKM2 and GLUT1 play a role in the activation process of qHSCs, experiments were conducted using recombinant proteins. The results indicated that both PKM2 and GLUT1 contribute to the enhancement of energy metabolism in qHSCs, thereby promoting activation (Supporting Information Fig. S11).

Further investigation was conducted through Western blot experiments to study the activation and collagen secretion of LX-2 cells after co-incubation with the extracted extracellular vesicles for 24 h. The LPS group exhibited a significantly elevated α-SMA and collagen-I level, indicating the activating effect of energy metabolism-related extracellular vesicles (Fig. 4D). However, for PF@HCZ, the collagen-1 content remained similar to the pretreatment level, while the levels of α-SMA even exhibiting a decreasing trend (Fig. 4D), which demonstrated that the treatment with PF@HCZ significantly reduced the activating effect of exosomes secreted by aHSCs on qHSCs. In addition, dose-dependent

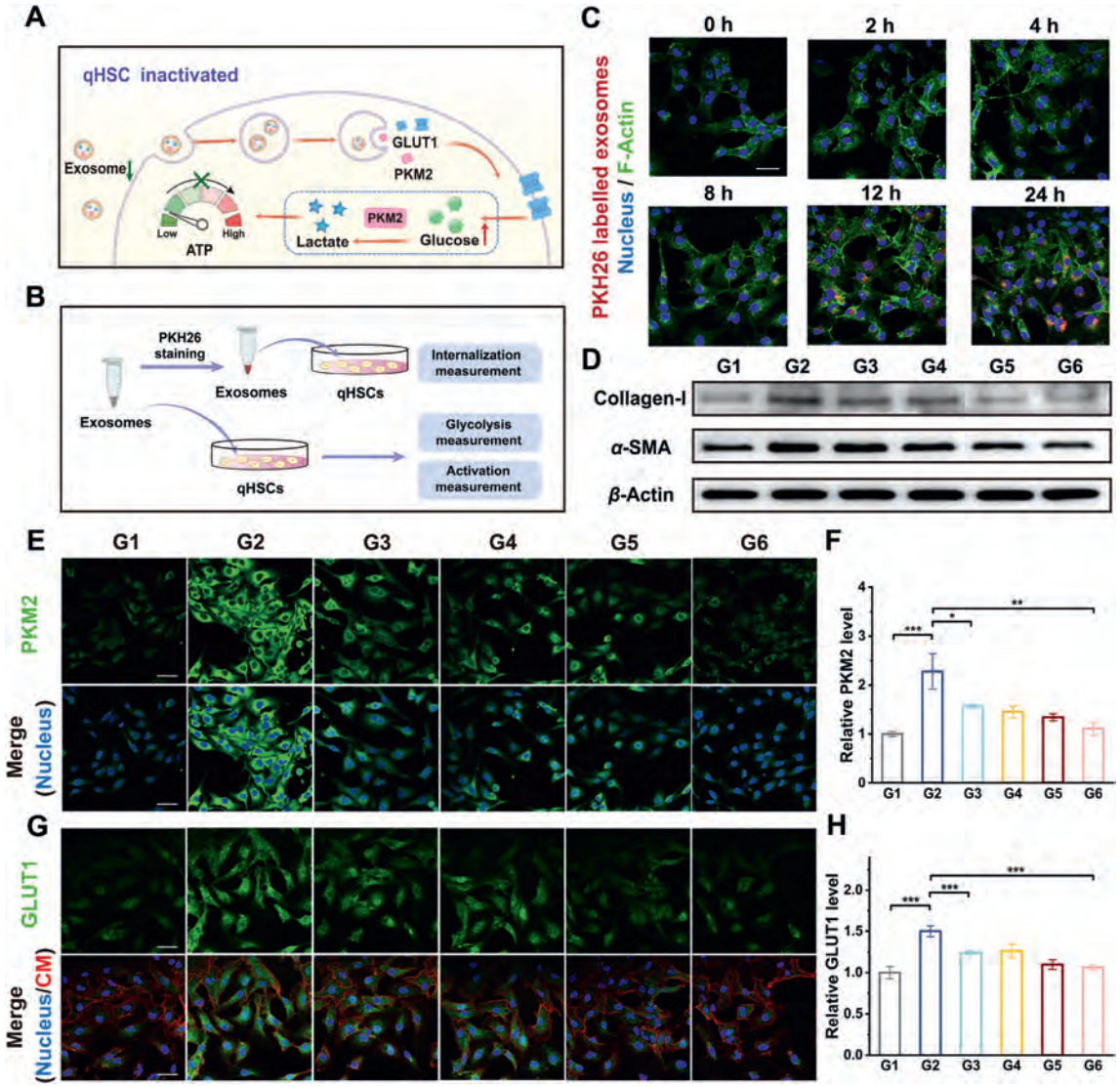

Figure 4 Inhibition of qHSCs activation by PF@HCZ *in vitro*. (A) Schematic illustration of the anti-fibrogenic mechanism of PF@HCZ regulates qHSCs activation by modulating exosomes. (B) Illustration of the method for exosome staining and verifying the effect for qHSCs activation. (C) CLSM micrographs showing the cellular uptake of PKH26-labeled exosomes from LX-2 cells (scale bar = 50 μm). (D) The expression of collagen-I and α-SMA after incubating with extracted exosomes. Fluorescent images of (E) PKM2 and (G) GLUT1 in LX-2 cells incubated with exosomes with nuclei in the blue and cellular membrane (CM) in red (scale bar = 50 μm). Mean fluorescence intensity of (F) PKM2 and (H) GLUT1 from Fig. 4E and G. Exosomes were obtained from the conditioned media of LX-2 cells treated with DMEM (Control) (G1), LPS (G2), LPS + PF (G3), LPS + HZ (G4), LPS + HCZ (G5), and LPS + PF@HCZ (G6). Data are shown as the mean ± SD ($n = 3$). NS (no significance), $^{*}P < 0.05$, $^{**}P < 0.01$, $^{***}P < 0.001$.

experiments demonstrated that the impact of exosomes on the activation of qHSCs progressively diminished with increasing dosage of PF@HCZ (Fig. S9B). In conclusion, it demonstrated *in vitro* that PF@HCZ inhibited the secretion of energy metabolism-related extracellular vesicles by aHSCs, thus disrupting intercellular communication mediated by exosomes and consequently slowing down extracellular vesicle-induced activation of qHSCs.

3.6. *In vivo biodistribution and targeting effect of PF@HCZ*

Next, DiR-loaded PF@HCZ was intravenously injected into mice, either healthy or with CCl_4-induced liver fibrosis, to assess the biodistribution and targeting specificity *in vivo* (Fig. 5A). In Fig. 5B, a significant deposition of DiR-loaded PF@HCZ was detected in the hepatic tissues of mice, both in healthy subjects and those with CCl_4-induced liver injury. The fluorescence signal persisted for 6 days in the healthy mice, while in the hepatic fibrosis group, a higher accumulation of the nanocarriers was evident with a prolonged duration (exceeding 8 days) owing to the impaired hepatic metabolic function resulting from liver fibrosis.

In addition, *ex vivo* fluorescent imaging of the major organs confirmed the accumulation of PF@HCZ in the liver. In the model group, the accumulation of PF@HCZ in the liver was 53.55 and 22.21 times higher than in the kidneys and lungs, respectively

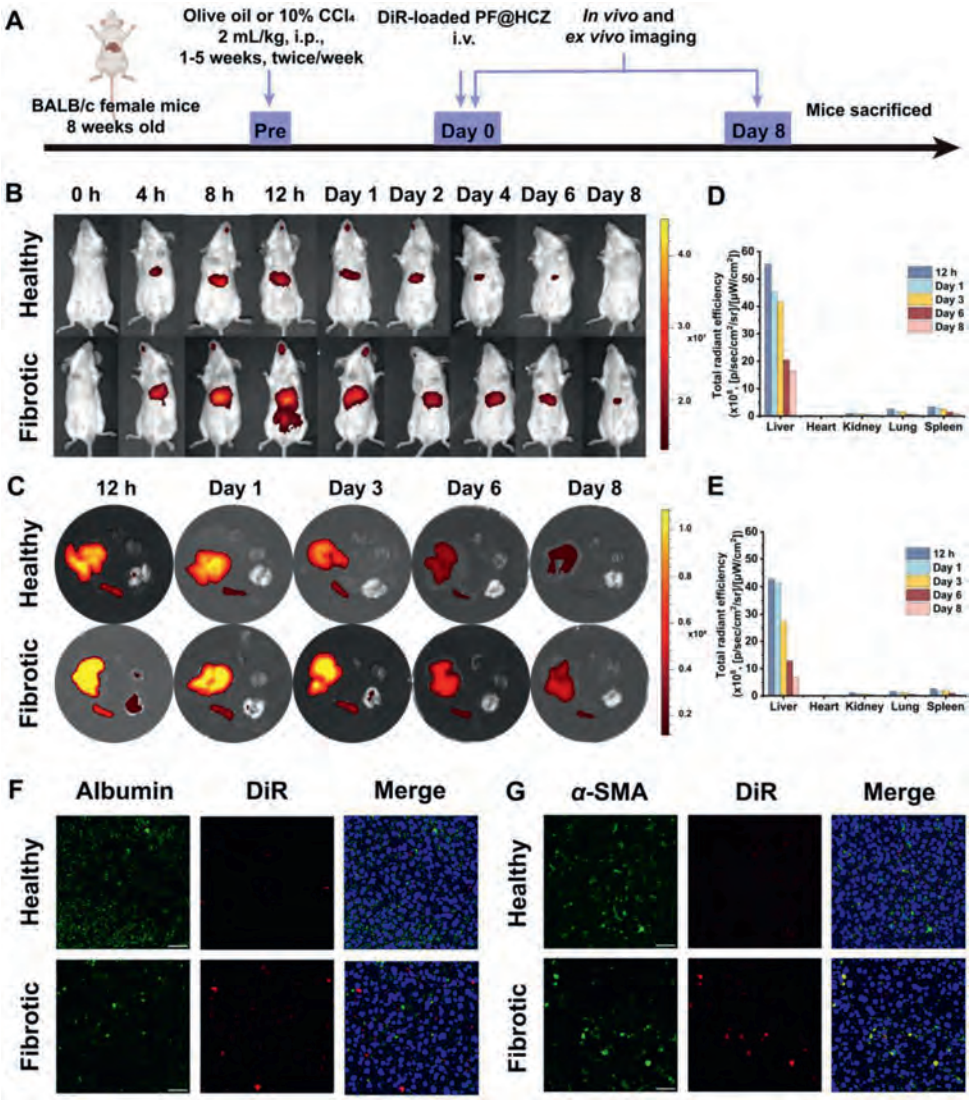

Figure 5 *In vivo* biodistribution and targeting effect of PF@HCZ. (A) Schematic diagram showing the induction of hepatic fibrosis by CCl_4 and the administration of DiR-loaded PF@HCZ in mice. (B) *In vivo* fluorescence imaging of healthy and fibrotic mice intravenously injected with DiR-loaded PF@HCZ at different times. (C) *Ex vivo* fluorescence imaging of the main organs from healthy and fibrotic mice intravenously injected with DiR-loaded PF@HCZ at different times. Quantitative analysis of *ex vivo* biodistribution of (D) fibrotic and (E) healthy mice. (F) and (G) Intrahepatic cell type-specific biodistribution of DiR-loaded PF@HCZ in normal and CCl_4-induced mice (scale bar = 100 μm). Data are shown as the mean ± SD (n = 3).

(Fig. 5C and D). For both the healthy and fibrotic groups, the signal in the kidneys, lungs, and spleen was less than one-tenth of that in the liver at each time point throughout the entire experimental duration (Fig. 5C−E), suggesting promising targeting capabilities. No signal was detected in the heart, which further confirmed the safety of the nanocarriers. These findings indicated that PF@HCZ exhibited promising targeting capabilities for effectively distributing within the liver.

Furthermore, liver tissue sections were collected after receiving DiR-loaded PF@HCZ for 24 h to investigate targeting ability and cell-specific distribution. As depicted in Fig. 5F and G, only facile red fluorescence can be observed in liver sections from normal mice, suggesting negligible uptake of DiR-loaded PF@HCZ. In contrast, liver sections from fibrotic mice displayed a stronger signal. Additionally, the red fluorescence of PF@HCZ extensively overlapped with the green fluorescence of HSCs (α-SMA positive) while maintaining a distinct separation from hepatocytes (albumin-positive), which indicated a specific affinity for HSC internalization. This observation suggested a significant portion of DiR-loaded PF@HCZ biological accumulation in the liver, particularly within aHSCs, confirming the superior targeting efficiency due to the surface HA modification.

3.7. *Liver fibrosis alleviation in vivo*

The liver fibrosis alleviation ability was evaluated in mice with the CCl_4-induced liver fibrosis model. For this purpose, BALB/c mice received intraperitoneal injection of CCl_4 (diluted with olive oil) for 8 weeks, followed by intravenous administration of different formulations twice a week from weeks 5−8 (Fig. 6A). First, H&E

staining revealed that the untreated fibrotic liver exhibited tissue proliferation and significant infiltration of inflammatory cells, while minimal heterotopic distribution was noted in the PF@HCZ and healthy groups (Fig. 6B). Moreover, these two groups also demonstrated a tighter cell arrangement, indicating alleviation of liver fibrosis. Quantitative analysis of ALT and AST confirmed that PF@HCZ administration promoted liver function recovery (Supporting Information Fig. S12). Activation of HSCs and collagen production are crucial parameters to be clarified during the progression of liver fibrosis, while Masson's staining, Sirius Red staining, and collagen-I immunohistochemistry were utilized to validate the levels of collagen deposition. Sirius Red staining showed that the collagen level in PF@HCZ treated mice was similar to that in the healthy mice, which was significantly lower compared to the CCl_4-induced group (Fig. 6C). Masson's staining revealed the extent of collagen deposition with muscle fibers appearing red and collagen fibers appearing blue, while the PF@HCZ exhibited a 65.45% decrease compared to the untreated groups (Fig. 6D and G). Additionally, collagen-I immunohistochemistry demonstrated reduced levels of collagen deposition in all treatment groups. Among these, PF@HCZ showed a notably more significant decrease compared to the other treatment groups, pointing to its optimal effectiveness in inhibiting collagen production in HSCs (Fig. 6E and H). The quantification of total hydroxyproline (Hyp) in liver tissue further corroborated the phenomenon of reduced collagen accumulation mediated by PF@HCZ (Supporting Information Fig. S13). Furthermore, the positive area of α-SMA in the model group was $8.21 \pm 0.79\%$ compared with only $4.04 \pm 0.45\%$ in the PF@HCZ group, suggesting that this nanocarrier effectively regulated the levels of α-SMA *in vivo* for suppressing HSC activation (Fig. 6F and I). In conclusion, our research indicated that disrupting exosome-mediated intercellular communication and energy metabolism of HSCs may be a potential therapeutic strategy.

3.8. Exosome interference and energy metabolism inhibition in vivo

Afterward, the intercellular communication interference effect of PF@HCZ was evaluated *in vivo*. First, the supernatant of liver tissue homogenates was obtained to assess levels of HK, LDH, and lactate. Following treatment, a significant reduction in the relative HK content of PF@HCZ group was noted, which was about 54.15% of that in the model group (Fig. 7A). Similarly, PF@HCZ exhibited a strong inhibitory effect on LDH in the tissue cells, showing a reduction of $\sim$31.50% compared to the model group (Fig. 7B). Furthermore, lactate decreased gradually from groups G2 to G6, reflecting the inhibitory effect of PF@HCZ on glycolysis which was induced by changes in HK and LDH levels (Fig. 7C). As depicted in Fig. 7E, HIF-1α was significantly overexpressed in the livers of mice from model group, while alleviation was observed after drug treatments in each group. Notably, the PF@HCZ group exhibited the most promising outcome, showing HIF-1α expression levels comparable to those in healthy mice. To differentiate the changes in the levels of PKM2 and GLUT1 as well as to verify the occurrence of glycolysis in HSCs, we conducted double-immunostaining of GFAP (a reliable marker for HSCs [47]) with PKM2 or GLUT1. As depicted in Fig. 7F and G, the PF@HCZ group exhibited comparable levels of GLUT1 and PKM2 expression to the healthy group, whereas a significant increase in expression was observed in the CCl_4-induced group. Moreover, the distinct co-localization of PKM2 and GLUT1 with GFAP (green signals) in the fibrotic group suggested an upregulation of glycolysis in HSCs during liver fibrosis, with a subsequent decrease in glycolysis following PF@HCZ administration. Ultimately, the alterations in ATP levels in liver tissues were assessed. The content in the CCl_4 group was approximately 1.3 times that of the PF@HCZ group, reaffirming the decline in cellular bioenergy and inhibitory effect of the nanocarrier on glycolysis at the disease site (Fig. 7D).

To determine whether the changes in PKM2 and GLUT1 were caused by exosomes, extracellular vesicles were extracted from the liver tissues of mice in different treatment groups for further exploration. The successful extraction was confirmed by observing typical cup-shaped vesicle structures in TEM images (Fig. 7H). The protein content of the exosomes was assessed utilizing a BCA assay kit, which showed a slight decrease in exosomal protein content in the PF@HCZ group compared to the CCl_4 group (Fig. 7I). NTA was employed to measure the particle concentration and particle size of the exosomes, where the concentration exhibited a similar trend to the protein content, indicating a certain inhibitory effect of PF@HCZ on exosomes (Supporting Information Fig. S14). Furthermore, the levels of glycolysis-related proteins in the extracted exosomes were examined using western blotting with the exosomal marker protein CD9 as loading control. The content of GLUT1 showed a decreasing trend from G2 to G6, with the content in exosomes from the PF@HCZ group being $\sim$40% of the model group (Fig. 7J). Additionally, there was a significant decrease in PKM2 content in the PF group and PF@HCZ group, which further confirmed the inhibitory effect of PF@HCZ on energy metabolism-related exosomes (Fig. 7J). In conclusion, the experiments above validated the inhibitory effect of PF@HCZ on glycolysis-related exosomes and bioenergy supply of aerobic glycolysis *in vivo*, indicating a decrease in the activation level of tissue HSCs after administration.

3.9. Safety assessment of PF@HCZ

Additionally, we conducted studies on *in vivo* metabolism and elimination. Following the tail vein injection, we observed that most PF@HCZ accumulated in the liver within 12 h, while the drug concentration in the blood gradually decreased. Based on the experiment data, decay equations [Eqs. (2) and (3)] were established to confirm the metabolic degradation of PF@HCZ (Supporting Information Fig. S15A and S15B):

$$y = 4.64e^{-\frac{t}{3.63}} + 0.10, R^2 = 0.990 \quad (2)$$

$$y = 0.56e^{-\frac{t}{3.68}} + 0.02, R^2 = 0.995 \quad (3)$$

Furthermore, we identified the primary excretion pathways of PF@HCZ. As depicted in Fig. S15C and S15D, PF@HCZ was eliminated by urine and feces, reaching peak levels between 12 and 24 h post-intravenous injection. Although an increase in the levels of Cu and Zn elements was detected in both urine and feces, fecal excretion emerged as the predominant pathway.

Further assessment of the safety profile of PF@HCZ was conducted. The levels of ALT and AST in the serum of the PF, HZ, HCZ, and PF@HCZ groups were comparable to those in the control group post-administration, which were lower than those in the CCl_4-induced group. The levels of ALT, ALP, TC, and ALB showed no significant differences compared to the healthy group (Fig. S12). Furthermore, results of CREA, UA, and urea levels suggested that PF@HCZ exhibited no nephrotoxicity (Fig. S12).

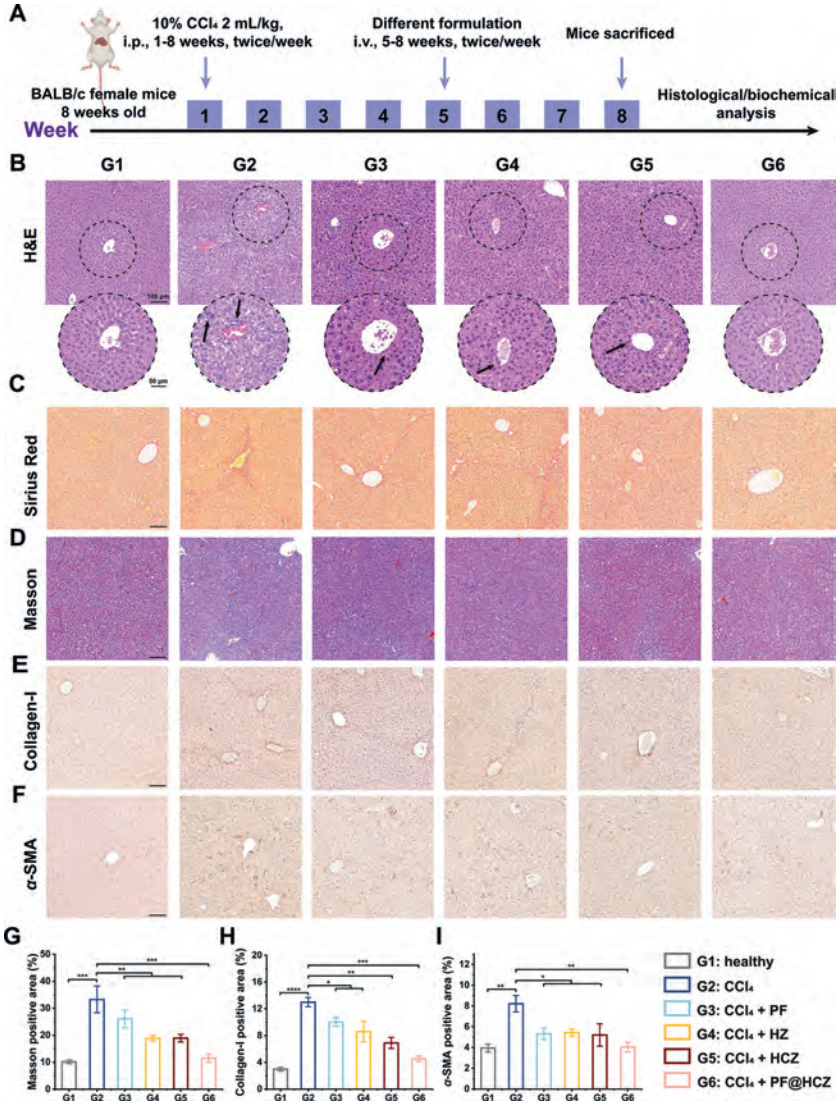

Figure 6 The effect of PF@HCZ on liver fibrosis alleviation. (A) Schematic diagram showing the induction of hepatic fibrosis by CCl_4 in mice and the administration with different formulations for therapy. (B) Representative images of liver slices from different groups after H&E staining (scale bar = 100 & 50 μm). (C) Sirius Red staining for collagen. (D) Masson staining results in various groups. (E) IHC staining of collagen-I. (F) IHC staining of α-SMA. Scale bar = 100 μm (Fig. 6C−F). (G) Quantitative analysis of Masson staining images in Fig. 6D. (H) Quantitative analysis of collagen-I in Fig. 6E. (I) Quantitative analysis of α-SMA in Fig. 6F. Control (G1), CCl_4 (G2), CCl_4 + PF (G3), CCl_4 + HZ(G4), CCl_4 + HCZ (G5), and CCl_4 + PF@HCZ(G6). Data are shown as the mean ± SD (n = 3). NS (no significance), $^*P < 0.05$, $^{**}P < 0.01$, $^{***}P < 0.001$.

Similarly, H&E staining revealed that PF@HCZ barely induced unexpected damage to the major organs of fibrotic mice (Supporting Information Fig. S16). Overall, these findings indicated that PF@HCZ possessed excellent biocompatibility and *in vivo* safety upon repeated intravenous injections.

In addition, during the modeling and treatment processes, we statistically analyzed the trends in body weight changes of the mice (Supporting Information Fig. S17). In healthy mice (G1), body weight gradually increases with age during the experimental course. Conversely, a decline in body weight was observed during the modeling phase in the model group and other treatment groups, possibly attributed to the acute toxicity of CCl_4. Following the administration of different treatments, the mice in the HP@HCZ group exhibited a more pronounced increase in body weight compared to the other treatment groups, registering a weight that was merely 1.04 g lower than that of the control group. However, mice in the model group had the lowest body weight, indicative of decreased appetite and metabolic alterations following the occurrence of hepatic fibrosis. Overall, all treatment groups illustrated an increase in body weight during the therapeutic phase, showing that the drugs did not elicit significant adverse reactions in the mice.

4. Conclusions

In this study, we have methodically devised a strategy to interfere with intercellular communication using a bimetallic MOF delivery system, which suppresses the secretion of energy metabolism-related exosomes to maintain both aHSCs and

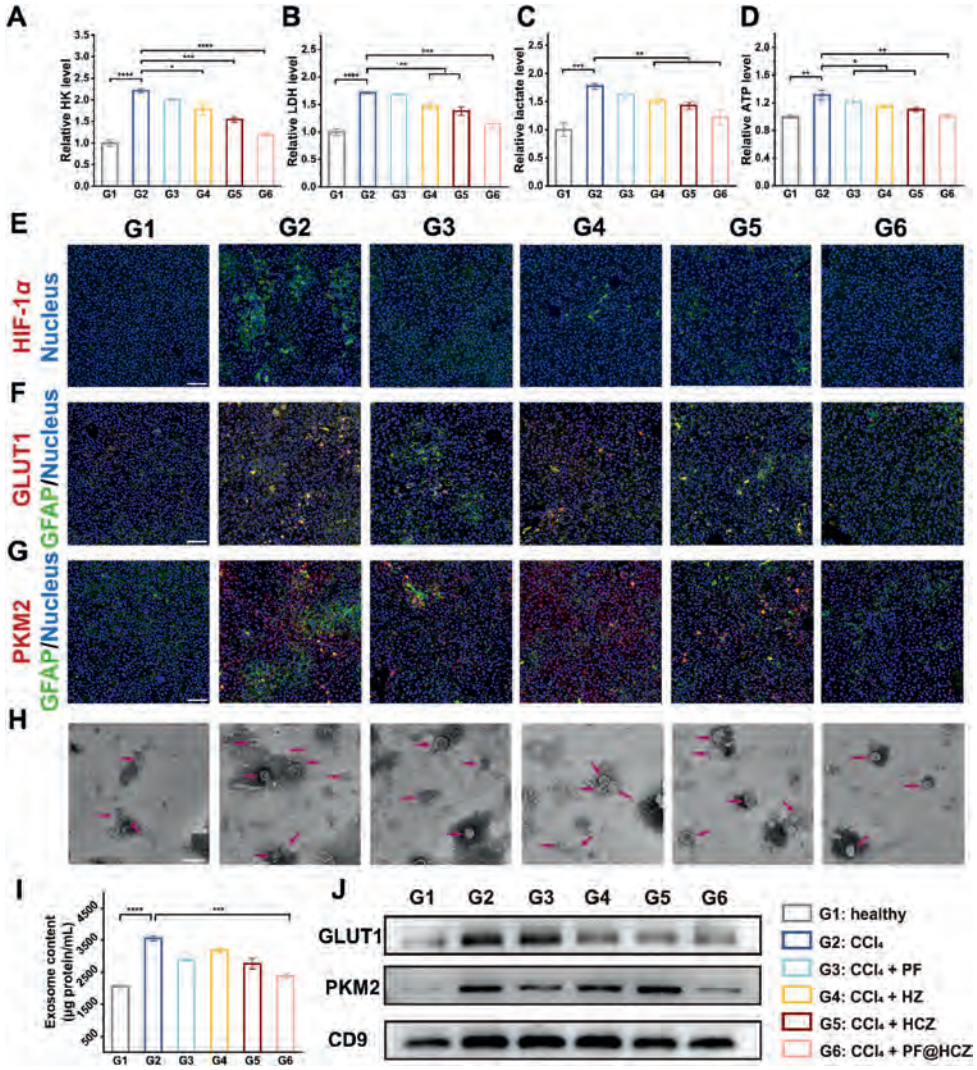

Figure 7 *In vivo* energy metabolism regulation effect and exosomes interference of PF@HCZ. (A) Relative HK level, (B) relative LDH content, (C) relative lactate level, and (D) relative ATP level in mice liver with different treatments. (E) Immunofluorescence of HIF-1α in liver tissue sections. Fluorescent images of hepatic (F) GLUT1 and (G) PKM2. Scale bar = 100 μm (Fig. 7E–G). (H) TEM image of the extracted exosomes (scale bar = 100 nm). (I) The protein content of extracted exosomes from mice liver. (J) Protein expressions of GLUT1 and PKM2 in exosomes. Control (G1), CCl_4 (G2), CCl_4 + PF (G3), CCl_4 + HZ(G4), CCl_4 + HCZ (G5), and CCl_4 + PF@HCZ (G6). Data are shown as the mean ± SD ($n = 3$). NS (no significance), $^*P < 0.05$, $^{**}P < 0.01$, $^{***}P < 0.001$, $^{****}P < 0.0001$.

qHSCs in a metabolically dormant state. Structurally, the outer layer encapsulated with HA can specifically target the upregulated CD44 receptor on the surface of aHSCs, while PF@HCZ releases Cu^{2+}, Zn^{2+}, and PF in a pH-responsive manner upon engulfment. The Cu^{2+} and Zn^{2+} selectively inhibit enzymes at different steps of glycolysis, reducing excessive bioenergy levels in aHSCs. Simultaneously, PF inhibits HIF-1α to decrease the secretion of energy metabolism-related exosomes, thereby protecting qHSCs from activation by exosomes and effectively inhibiting the progression of liver fibrosis. Through *in vitro* and *in vivo* studies, we have validated that PF@HCZ regulates energy metabolism by inhibiting exosome secretion, ultimately preventing HSC activation to ameliorate liver fibrosis. Therefore, the strategy of interfering with intercellular communication provides valuable insights for the treatment of liver fibrosis.

Acknowledgments

This work was supported by the National Natural Science of China (82273873 and 31971106, China), the Youth Science and Technology Talent Program by Tianjin (QN20230215, China), the National Key Research and Development Program of China (2020YFC1512304 and 2020YFC1512301, China), the Tianjin Natural Science Foundation (24JCZDJC01110 China), and the Major Special Projects (0402080005, China).

Author contributions

Mengyao Zhang: Conceptualization, Investigation, Methodology, Writing–original draft. Huaqing Jing: Investigation, Methodology, Writing–review & editing. Xinyi Liu: Investigation,

Software, Visualization. Valentin A. Milichko and Yunsheng Dou: Investigation, Methodology. Yingzi Ren, Zitong Qiu, and Wen Li: Investigation, Software. Weili Liu and XinXing Wang: Funding acquisition, Supervision. Nan Li: Conceptualization, Supervision, Funding acquisition, Writing−review & editing. All of the authors have read and approved the final manuscript.

Conflicts of interest

The authors have no conflicts of interest to declare.

Appendix A. Supporting information

Supporting information to this article can be found online at https://doi.org/10.1016/j.apsb.2025.07.008.

References

1. Marcellin P, Kutala BK. Liver diseases: a major, neglected global public health problem requiring urgent actions and large-scale screening. *Liver Int* 2018;**38**:2−6.
2. Koyama Y, Xu J, Liu X, Brenner DA. New developments on the treatment of liver fibrosis. *Dig Dis* 2016;**34**:589−96.
3. Tan Z, Sun HB, Xue TX, Gan CL, Liu HY, Xie YT, et al. Liver fibrosis: therapeutic targets and advances in drug therapy. *Front Cell Dev Biol* 2021;**9**:730176.
4. Zhao X, Kwan JYY, Yip K, Liu PP, Liu FF. Targeting metabolic dysregulation for fibrosis therapy. *Nat Rev Drug Discov* 2020;**19**: 57−75.
5. Delgado ME, Cárdenas BI, Farran N, Fernandez M. Metabolic reprogramming of liver fibrosis. *Cells* 2021;**10**:3604.
6. Khomich O, Ivanov AV, Bartosch B. Metabolic hallmarks of hepatic stellate cells in liver fibrosis. *Cells* 2020;**9**:24.
7. Lee UE, Friedman SL. Mechanisms of hepatic fibrogenesis. *Best Pract Res Clin Gastroenterol* 2011;**25**:195−206.
8. Liu YF, Zheng YH, Yang Y, Liu K, Wu JY, Gao PY, et al. Exosomes in liver fibrosis: the role of modulating hepatic stellate cells and immune cells, and prospects for clinical applications. *Front Immunol* 2023;**14**: 1133297.
9. He CB, Zheng S, Luo Y, Wang B. Exosome theranostics: biology and translational medicine. *Theranostics* 2018;**8**:237−55.
10. Mastoridou EM, Goussia AC, Glantzounis GK, Kanavaros P, Charchanti AV. Autophagy and exosomes: cross-regulated pathways playing major roles in hepatic stellate cells activation and liver fibrosis. *Front Physiol* 2022;**12**:801340.
11. Masyuk AI, Masyuk TV, Larusso NF. Exosomes in the pathogenesis, diagnostics and therapeutics of liver diseases. *J Hepatol* 2013;**59**: 621−5.
12. Geerts A. History, heterogeneity, developmental biology, and functions of quiescent hepatic stellate cells. *Semin Liver Dis* 2001;**21**: 311−35.
13. Malarkey DE, Johnson K, Ryan L, Boorman G, Maronpot RR. New insights into functional aspects of liver morphology. *Toxicol Pathol* 2005;**33**:27−34.
14. Raposo G, Stoorvogel W. Extracellular vesicles: exosomes, microvesicles, and friends. *J Cell Biol* 2013;**200**:373−83.
15. Chen L, Charrier A, Zhou Y, Chen RJ, Yu B, Agarwal K, et al. Epigenetic regulation of connective tissue growth factor by MicroRNA-214 delivery in exosomes from mouse or human hepatic stellate cells. *Hepatology* 2014;**59**:1118−29.
16. Li XL, Chen RJ, Kemper S, Brigstock DR. Dynamic changes in function and proteomic composition of extracellular vesicles from hepatic stellate cells during cellular activation. *Cells* 2020;**9**:290.
17. Charrier A, Chen RJ, Chen L, Kemper S, Hattori T, Takigawa M, et al. Exosomes mediate intercellular transfer of pro-fibrogenic connective tissue growth factor (CCN2) between hepatic stellate cells, the principal fibrotic cells in the liver. *Surgery* 2014;**156**:548−55.
18. Wan L, Xia T, Du YQ, Liu J, Xie YY, Zhang YJ, et al. Exosomes from activated hepatic stellate cells contain GLUT1 and PKM2: a role for exosomes in metabolic switch of liver nonparenchymal cells. *FASEB J* 2019;**33**:8530−42.
19. Han J, He YP, Zhao H, Xu XW. Hypoxia inducible factor-1 promotes liver fibrosis in nonalcoholic fatty liver disease by activating PTEN/p65 signaling pathway. *J Cell Biochem* 2019;**120**:14735−44.
20. Hou W, Syn W-K. Role of metabolism in hepatic stellate cell activation and fibrogenesis. *Front Cell Dev Biol* 2018;**6**:00150.
21. Smith-Cortinez N, van Eunen K, Heegsma J, Serna-Salas SA, Sydor S, Bechmann LP, et al. Simultaneous induction of glycolysis and oxidative phosphorylation during activation of hepatic stellate cells reveals novel mitochondrial targets to treat liver fibrosis. *Cells* 2020;**9**: 2456.
22. Sun XY, Peng YJ, Zhao JD, Xie ZZ, Lei XY, Tang GT. Discovery and development of tumor glycolysis rate-limiting enzyme inhibitors. *Bioorg Chem* 2021;**112**:104891.
23. Ehrke E, Arend C, Dringen R. 3-Bromopyruvate inhibits glycolysis, depletes cellular glutathione, and compromises the viability of cultured primary rat astrocytes. *J Neurosci Res* 2015;**93**:1138−46.
24. Clem B, Telang S, Clem A, Yalcin A, Meier J, Simmons A, et al. Small-molecule inhibition of 6−phosphofructo−2−kinase activity suppresses glycolytic flux and tumor growth. *Mol Cancer Ther* 2008; **7**:110−20.
25. Lai JCK, Blass JP. Neurotoxic effects of copper: inhibition of glycolysis and glycolytic enzymes. *Neurochem Res* 1984;**9**:1699−710.
26. Da Silva E, Kembouche Y, Tegner U, Baun A, Jensen KA. Interaction of biologically relevant proteins with ZnO nanomaterials: a confounding factor for *in vitro* toxicity endpoints. *Toxicol Vitro* 2019;**56**:41−51.
27. Sunanda Rao BSS, Raju TR. Corticosterone attenuates zinc-induced neurotoxicity in primary hippocampal cultures. *Brain Res* 1998;**791**: 295−8.
28. Haase H, Rink L. Multiple impacts of zinc on immune function. *Metallomics* 2014;**6**:1175−80.
29. Grüngreiff K, Gottstein T, Reinhold D. Zinc in liver fibrosis. *OBM Hepatol Gastroenterol* 2019;**3**:18.
30. Li WH, Zhou CC, Fu Y, Chen TJ, Liu X, Zhang ZR, et al. Targeted delivery of hyaluronic acid nanomicelles to hepatic stellate cells in hepatic fibrosis rats. *Acta Pharm Sin B* 2020;**10**:693−710.
31. Zhao YL, Ma X, Wang JB, Zhu Y, Li RS, Wang J, et al. Paeoniflorin alleviates liver fibrosis by inhibiting HIF-1α through mTOR-dependent pathway. *Fitoterapia* 2014;**99**:318−27.
32. Bian XL, Jiang HF, Meng Y, Li YP, Fang J, Lu ZM. Regulation of gene expression by glycolytic and gluconeogenic enzymes. *Trends Cell Biol* 2022;**32**:786−99.
33. Sakthivel R, Prasanna SB, Tseng CL, Lin LY, Duann YF, He JH, et al. A sandwich-type electrochemical immunosensor for insulin detection based on Au-adhered Cu_5Zn_8 hollow porous carbon nanocubes and AuNP deposited Nitrogen-doped holey graphene. *Small* 2022;**18**:2202516.
34. Wang ZX, Zhou P, Li YT, Zhang D, Chu FC, Yuan F, et al. A bimetallic polymerization network for effective increase in labile Iron pool and robust activation of cGAS/STING induces Ferroptosis-based tumor immunotherapy. *Small* 2024;**20**:2308397.
35. Amur SA, Soomro NA, Khuhro Q, Wei Y, Liang H, Yuan QP. Encapsulation of natural drug gentiopicroside into zinc based Zeolitic Imidazolate Frameworks (ZIF-8): *in-vitro* drug release and improved antibacterial activity. *J Drug Deliv Sci Technol* 2023;**84**:104530.
36. Yu SX, Wang SY, Xie ZK, Yu SY, Li L, Xiao HF, et al. Hyaluronic acid coating on the surface of curcumin-loaded ZIF-8 nanoparticles for improved breast cancer therapy: an *in vitro* and *in vivo* study. *Colloids Surf, B* 2021;**203**:111759.
37. Théry C, Witwer KW, Aikawa E, Alcaraz MJ, Anderson JD, Andriantsitohaina R, et al. Minimal information for studies of extracellular vesicles 2018 (MISEV2018): a position statement of the International Society for Extracellular Vesicles and update of the MISEV2014 guidelines. *J Extracell Vesicles* 2018;**7**:1535750.

38. Sun ZJ, Ji SR, Wu JL, Tian JL, Quan WQ, Shang AQ, et al. Proteomics-based identification of candidate exosomal glycoprotein biomarkers and their value for diagnosing colorectal cancer. *Front Oncol* 2021;**11**:725211.
39. Song YZ, Han S, Liu SW, Sun RN, Zhao L, Yan C. Biodegradable imprinted polymer based on ZIF-8/DOX-HA for synergistically targeting prostate cancer cells and controlled drug release with multiple responses. *ACS Appl Mater Interfaces* 2023;**15**:25339−53.
40. Obaid E, Wu S, Zhong Y, Yan M, Zhu L, Li BB, et al. pH-Responsive hyaluronic acid-enveloped ZIF-8 nanoparticles for anti-atherosclerosis therapy. *Biomater Sci* 2022;**10**:4837−47.
41. Sun SW, Yang ZH, Cao J, Wang Y, Xiong WP. Copper-doped ZIF-8 with high adsorption performance for removal of tetracycline from aqueous solution. *J Solid State Chem* 2020;**285**:121219.
42. Ji Y, Wang T, Wei ZF, Lu GX, Jiang SD, Xia YF, et al. Paeoniflorin, the main active constituent of Paeonia lactiflora roots, attenuates bleomycin-induced pulmonary fibrosis in mice by suppressing the synthesis of type I collagen. *J Ethnopharmacol* 2013; **149**:825−32.
43. Chen XL, Liu C, Lu YF, Yang ZG, Lv Z, Xu QN, et al. Paeoniflorin regulates macrophage activation in dimethylnitrosamine-induced liver fibrosis in rats. *BMC Compl Alternative Med* 2012;**12**:254.
44. Jiang DH, Liang JR, Fan J, Yu S, Chen SP, Luo Y, et al. Regulation of lung injury and repair by Toll-like receptors and hyaluronan. *Nat Med* 2005;**11**:1173−9.
45. Satoh T, Ichida T, Matsuda Y, Sugiyama M, Yonekura K, Ishikawa T, et al. Interaction between hyaluronan and CD44 in the development of dimethylnitrosamine-induced liver cirrhosis. *J Gastroenterol Hepatol* 2000;**15**:402−11.
46. Yang YM, Noureddin M, Liu C, Ohashi K, Kim SY, Ramnath D, et al. Hyaluronan synthase 2-mediated hyaluronan production mediates Notch1 activation and liver fibrosis. *Sci Transl Med* 2019;**11**: eaat9284.
47. Castilho-Fernandes A, de Almeida DC, Fontes AM, Melo FUF, Picanço-Castro V, Freitas MC, et al. Human hepatic stellate cell line (LX-2) exhibits characteristics of bone marrow-derived mesenchymal stem cells. *Exp Mol Pathol* 2011;**91**:664−72.